small methods
www.small-methods.com

Octylammonium Iodide Induced In-situ Healing at "perovskite/Carbon" Interface to Achieve 85% RH-moisture Stable, Hole-Conductor-Free Perovskite Solar Cells with Power Conversion Efficiency >19%

*Siyuan Lin, Zhenxing Fang, Jiao Ma, De'en Guo, Xiaohan Yu, Haipeng Xie, Mei Fang, Dou Zhang, Kechao Zhou, Yongli Gao, and Conghua Zhou**

"Perovskite/carbon" interface is a bottle-neck for hole-conductor-free, carbon-electrode basing perovskite solar cells due to the energy mismatch and concentrated defects. In this article, in-situ healing strategy is proposed by doping octylammonium iodide into carbon paste that used to prepare carbon-electrode on perovskite layer. This strategy is found to strengthen interfacial contact and reduce interfacial defects on one hand, and slightly elevate the work function of the carbon-electrode on other hand. Due to this effect, charge extraction is accelerated, while recombination is obviously reduced. Accordingly, power conversion efficiency of the hole-conductor-free, planar perovskite solar cells is upgraded by ≈50%, or from 11.65 (± 1.59) % to 17.97 (± 0.32) % (AM1.5G, 100 mW cm^{-2}). The optimized device shows efficiency of 19.42% and open-circuit voltage of 1.11 V. Meanwhile, moisture-stability is tested by keeping the unsealed devices in closed chamber with relative humidity of 85%. The "in-situ healing" strategy helps to obtain T_{80} time of >450 h for the carbon-electrode basing devices, which is four times of the reference ones. Thus, a kind of "internal encapsulation effect" has also been reached. The "in situ healing" strategy facilitates the fabrication of efficient and stable hole-conductor-free devices basing on carbon-electrode.

1. Introduction

The photo-to-electric power conversion efficiency (PCE) of perovskite solar cells (PSCs) has been improved from the initial 3.81% to 26.1% during the past decades.[1–5] Industrialization has become a hot topic, although the stability problems have not been thoroughly solved.[6] Part of those problems stem from the pristine nature of the organic–inorganic hybrid perovskite (PVSK) material, for example, the corrosion to metal electrodes (such as Ag and Al),[7,8] and the environment-sensitive nature of some hole-transport-material (HTM, such as spiro-OMeTAD).[9,10] Carbon-electrodes have been used to replace metallic ones in the early stages of PSCs research, due to their robustness against electrochemical corrosion and excellent conductivity.[11] Carbon-electrode was suggested to own relatively higher work function (4.6–5.0 eV) than Ag (4.35 eV) or Al (4.31 eV),[12] making it possible to achieve power conversion for PSCs, even without the assistance of HTM. This has led to the development of carbon-electrode basing, hole-conductor-free PSCs (or CPSCs for short). Besides, carbon-electrode is cost-effective, and somehow hydrophobic, which could lower down production cost, and improve device stability. During the past 10 years, several types of CPSCs have been designed, including mesoscopic,[13] embedment,[14] planar[15]/quasi-planar structured devices.[16] Through device structure optimization and crystallization manipulation, the PCE has risen from 6.64% to 18.82% for mesoscopic CPSCs,[11,13,17] and from 8.31% to 18.9% for planar ones.[18–20] Giving a relatively large gap of PCE, device stability has become a major merit for the CPSCs due to the inert and hydrophobic nature of carbon-electrodes. For example, Han's group observed over 9000 h operational stability in mesoscopic CPSCs,[21] and our group has also observed storage stability up to 5 months in planar CPSCs.[15]

Planar CPSCs have a similar architecture to metal-electrode basing devices. The main difference comes from the lack of one more layer of HTM. This means that the PVSK layer must face

S. Lin, Z. Fang, J. Ma, D. Guo, X. Yu, H. Xie, M. Fang, C. Zhou
Hunan Key Laboratory of Super-microstructure and Ultrafast Process, Hunan Key Laboratory of Nanophotonics and Devices, Institute of Super-microstructure and Ultrafast Process in Advanced Materials (ISUPAM), School of Physics and Electronics
Central South University
Changsha, Hunan 410083, P. R. China
E-mail: chzhou@csu.edu.cn

D. Zhang, K. Zhou
State Key Laboratory of Powder Metallurgy, Powder Metallurgy Research Institute
Central South University
Changsha, Hunan 410083, P. R. China

Y. Gao
Department of Physics and Astronomy
University of Rochester
Rochester, NY 14627, USA

The ORCID identification number(s) for the author(s) of this article can be found under https://doi.org/10.1002/smtd.202300716

DOI: 10.1002/smtd.202300716

directly to carbon-electrode. This unique structure brings several challenges to the power conversion process, such as loose interface contact, energy level mismatch, and concentrated defects. To solve these problems, several methods have been attempted. For example, Yan et al. in 2019 treated the whole device of planar CPSC by a moisture-assisted post-annealing technique, and observed that the treatment could trigger a secondary round growth of PVSK, which then reduced the gap between the interface of "PVSK/Carbon".[15] Ma et al. in 2020 reported that acetylene black could also reduce the interfacial gap, and improved the efficiency to 16.41%.[22] Besides, hot-pressing has also been practiced.[23]

To reduce the energy level mismatch, adding HTM has proven to be an efficient strategy for CPSCs. For example, Meng et al. in 2018 developed a kind of self-adhesive macroporous carbon-electrode, and imported spiro-OMeTAD as the HTM, after which they obtained a PCE of 19.2% for CPSCs.[24] In 2021, they further improved the PCE up to 20.04% through component engineering on PVSK.[25] Besides, Yang et al. introduced Poly(3-hexylthiophene-2,5-diyl) (P3HT) between PVSK and carbon-electrode to improve charge transport process, and achieved certified PCE of 17.8%.[26] Grätzel et al. applied CuSCN as HTM between carbon-electrode and PVSK, and achieved a PCE of 18.1%.[27] Tan et al. designed NiOx/P3HT as HTM between carbon-electrode and PVSK, which realized a PCE of 20.14%.[28] Recently and impressively, Shi et al. promoted the PCE to 22.07% by introducing defective carbon-nanotube (CNT)-doped spiro-OMeTAD as HTM.[29]

To reduce interface defects between "PVSK/ carbon" interface, several approaches have been proposed. For example and recently, Kim et al. coated thin layer of 2D molecule of octylammonium iodide (OAI) on PVSK, which helped to form 2D phase PVSK on the surface, and achieve a PCE of 18.5% for planar CPSCs.[30] Han et al. observed that δ-$FAPbI_3$ formed at "PVSK/carbon" interface could suppress charge recombination, and help to obtain a PCE of 17.11% for mesoscopic CPSCs.[31] Priya et al. observed that perfluorotetradecanoic acid could help to reduce defects in PVSK, and obtain PCE of 18.9% for planar CPSCs.[20] Besides, increasing work function (WF) of carbon-electrode is also efficient to upgrade device efficiency. For example, Yang et al. in 2017 regulated the WF of carbon-electrode by doping boron in multi-walled carbon nanotubes, and improved PCE from 10.70% to 15.23% for embedment CPSCs.[32] Han et al. in 2018 increased the WF of carbon-electrode from 5.0 to 5.2 eV through oxygen management, and improved device efficiency of mesoscopic CPSCs.[33] However, one should be aware of that the PCE of CPSCs is still lower than metal electrode devices,[34] especially for the HTM-free ones, thus more works are needed.

Recently, 2D PVSK has emerged as an efficient passivation layer for 3D PVSK.[35–37] Here in this work, a kind of in-situ healing strategy is proposed to modify "PVSK/carbon" interface. OAI is doped in carbon paste that is used to prepare carbon-electrode on PVSK. As will be shown later, the strategy efficiently reduces the interfacial trap states, strengthens interface contact, and also slightly increases the work function of the carbon-electrode, which then improves the efficiency from 11.65 (± 1.59) % to 17.97 (± 0.32) % (optimized at 19.42%). Moreover, OAI treatment strengthens moisture resistance of CPSCs, even when being treated in heavy humidity environment (relative humidity of 85%).

2. Results and Discussion

2.1. OAI induced "In-situ Healing" Behavior at "Perovskite/Carbon" Interface

Fabrication process of planar CPSCs is shown in **Figure 1**a–d. Typically, it adopts a kind of "bottom-up" process, or carbon paste is coated on top of PVSK, to make direct contact with the active layer. As such, solvent of carbon paste should be inert to PVSK.[26] Previously, Terpineol and Tetron [the main components are 2-(2-Ethoxyethoxy) ethyl acetate] have been used as solvents for experimental or commercial carbon pastes. As is shown in Figure S1 (Supporting Information), both of the two solvents could dissolve PVSK in 1.5 h, while terpineol acts more quickly. In contrast, IPA shows the weakest solubility to PVSK. Besides, IPA is wettable to both OAI and organic binders of hydroxypropyl cellulose (Figure S2, Supporting Information). As a result, IPA is used as the solvent in carbon paste. To perform the in-situ healing strategy, OAI is doped in carbon paste during the ball milling process. To make meaningful comparison, different amounts of OAI are added to certain volume (25 mL) carbon paste, for example, 0, 40, 80, 160, and 320 mg, respectively. Planar CPSCs with structure of "FTO/SnO_2/PVSK/Carbon-electrode" are fabricated, following the procedure described in Figure 1a–d. Details are referred to Experimental Section. The carbon-electrode is fabricated in open air and the whole fabrication process is performed at a relative low temperature (≤150 °C). Figure 1e shows a cross-sectional image of one typical CPSC.

The PVSK materials are known by the rigid and sensitive nature to moisture. To improve the moisture stability, "sealing" technique is usually adopted for PSCs. However, as for CPSCs, the requirement might not be so urgent. For example, in current study, the hydrophobicity of carbon-electrode could be improved by OAI doping. This could be reflected by testing the contact angle (water is used as the test reagent). As shown in **Figure 2**a, contact angle is 36.2° for pristine carbon-electrode, it increases to 55.8° after 160 mg OAI is doped, and the contact angle increases with the concentration of OAI. The increased hydrophobicity is induced by hydrophobic carbon chains of OAI molecules. Conductivity of the carbon-electrode is also tested. As is shown in Figure S3 (Supporting Information), OAI affects little to the conductivity. To study the effect of OAI on chemical and electronic properties of carbon-electrode, Fourier transform infrared (FTIR) is adopted, the results are shown in Figure 2b. The absorption peak at 1110.12 cm^{-1} is due to the stretch mode of "C—O" group at carbon particles. According to literature, such group usually comes from the surface hydroxyl of "C—OH".[38] It shifts to 1113.02 cm^{-1} after OAI doping, indicating possible interaction between OAI and carbon particles. X-ray photoelectron spectra (XPS) are also performed. The full XPS spectrum of carbon-electrode is shown in Figure S4 (Supporting Information). As shown in Figure 2c, the I3d peak of pristine OAI molecule is located at binding energy of 619.82 eV, it moves to 619.15 eV after mixing with carbon powder, leading to a negative shift of 0.67 eV. Similar behavior is observed for N1s. It is 402.83 eV for pristine OAI, then shifting to 402.06 eV after mixing with carbon (Figure 2d). The negative shift is due to the interaction between OAI and carbon particles. XPS study is also performed on pure graphite and carbon black. As shown in Figure 2e,f, for the

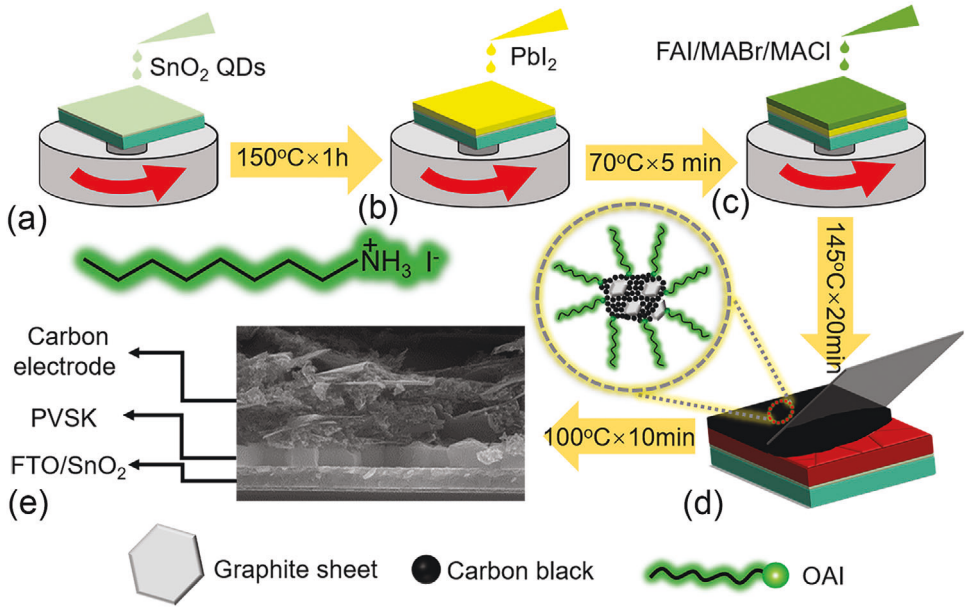

Figure 1. Schematic diagram for the fabrication of planar CPSCs: a) SnO_2, b) PbI_2, c) organic salt layer, and d) carbon electrode. e) Cross-sectional scanning electron microscope (SEM) image of a typical CPSC. Note that OAI is doped in the carbon paste.

C1s, the binding energy of 284, 285, and 286 eV is due to carbon atoms from groups of C—C, C—O, and C═O, respectively.[39] For O1s, peaks of binding energy at ≈532 and 533 eV are due to the oxygen atoms from group of C═O/C—O—C, and C—OH, respectively.[40,41] In more, from Figure 2f, one can find that, there are more surface hydroxyl groups (—OH) on carbon black nanoparticles. Thus, hydrogen bond is easy to form between these groups and [R-NH_3^+] end of OAI. As is shown by the schematic diagram in Figure 2h, surface group of C—OH could also interact with I & N atoms from OAI molecules, increasing the electron density around them. The increased density strengthens the "shielding effect", which decreases the binding energy of atomic nucleus to core level electrons (or leads to a negative shift on the binding energy).[42]

Work function (WF) of carbon-electrode is tested by ultraviolet photoelectron spectrum (UPS). The second cut-off edge is presented in Figure 2g. WF is calculated according to Equation (1):

$$WF = h\nu - E_{cut-off} \quad (1)$$

It is 4.45 eV for pristine carbon-electrode, 4.5 eV after 160 mg OAI doping (as reference, Au with WF of 4.81 eV is also shown). Thus, a slight increment of 0.05 eV is observed. The slightly increased WF is due to the interaction between OAI and carbon particles. First, I atom is highly electronegative, thus is favorable for the WF elevation. Secondary, it is well-known that N-containing groups could interact with surface carbon atoms (or edge, as shown in Figure 2h), and reduce the dangling bonds or defects brought by these under-coordination carbon atoms.[43] The reduced defect could also improve the WF. The elevated WF could reduce the mismatch in interfacial energy levels, and favor the interfacial charge transfer while retard charge recombination. The merits will be clearly reflected by the following sections. Besides, the increased WF also coincides with the negative shift observed in XPS study, like that discussed before.[44] It is also noting that, more works are needed to examine the effect of halogen atom/ions on the WF of carbon-electrode.

Cross-sectional SEM images of the CPSCs are shown in **Figure 3**a. Film thickness of the carbon-electrodes is from 8.52 to 13.29 μm as revealed by Figure S3 (Supporting Information). During the drying process of carbon paste, OAI molecules-doped in carbon paste could react with the PVSK lying beneath, and form 2D phase PVSK at the interface between 3D PVSK and carbon-electrode. To make the reaction visible, and also to eliminate the influence of the thick carbon-electrode itself, OAI/IPA solution with the same concentration in carbon paste is spin-coated on surface of PVSK, and then dried and characterized by XRD. The resultant patterns are shown in Figure 3b. It is observed that, with OAI concentration increasing, the intensity of the peak at 12.7° (corresponding to PbI_2) decreases, in contrast, another small diffraction angle lying at ˜4.7° (corresponding to 2D PVSK) increases.[45] Such phenomenon shows that, 2D phase PVSK are formed after OAI doping. Due to the formation of 2D PVSK, residual PbI_2 is reduced. The formation of 2D PVSK is also monitored by XPS. As shown in Figure 3c,d, N1s at low binding energy of ≈401.6 eV (401.54 and 401.64 eV) is assigned to —NH_2 of FA in PVSK; additional peak lying at binding energy of 403.04 eV is from the —NH_3 of octylammonium (from OAI) in the 2D PVSK.[30] As for Pb4f spectra, the 3D perovskite film exhibited main peaks at 139.54 and 144.49 eV. After OAI doping, the peaks shift to 139.90 and 144.77 eV, respectively (Figure 3d).[46] The formation of 2D PVSK at "PVSK/carbon" interface is further checked by high-resolution transmission electron microscope (HRTEM). As is shown in Figure 3e, focused ion beam (FIB) technology is used to pick the interface region between "PVSK/carbon". From the HRTEM image shown in Figure 3f, one can distinguish three nano-structures: carbon, 2D PVSK particles with interplanar spacing of 0.78 nm, and

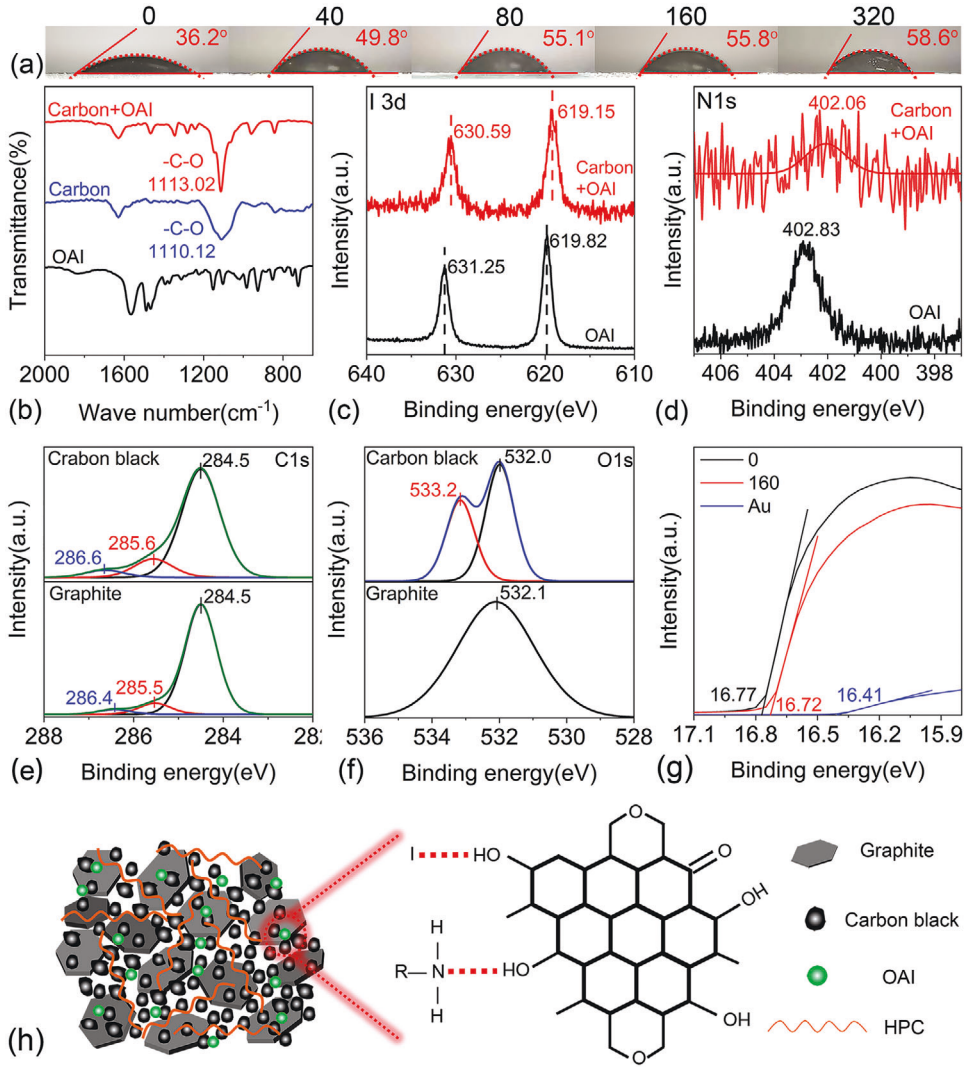

Figure 2. a) Contact angle test of carbon-electrode. b) Fourier transform infrared spectroscopy (FTIR) study on OAI, and carbon-powder doped with OAI or not. X-ray photoelectron spectrum (XPS) of carbon-electrode-doped with OAI or not: c) N1s, d) I3d. XPS of pure graphite and carbon black powder: e) C1s, f) O1s. g) Ultraviolet photoelectron spectrum (UPS) of carbon-electrode-doped with OAI or not. h) Schematic diagram to show the interaction between carbon-electrode and OAI molecule.

3D PVSK with interplanar spacing of 0.32 nm.[47] As a result, a thin layer of 2D PVSK has been formed between 3D PVSK and carbon-electrode, making closely packed "PVSK/carbon" interface. Similar to previous studies, the formation of 2D phase layer could reduce surface defects of 3D PVSK, thus suppressing interfacial charge recombination, and favor the power conversion processes.[48,49]

From the above presentation, one can see that, OAI doping could bring three main merits: i) Interfacial contact between PVSK and carbon-electrode is strengthened by the formation of 2D PVSK, and defects of PVSK are reduced; ii) Defects on carbon particles are reduced due to the interaction between OAI molecules and carbon, and WF of the carbon-electrode is slightly elevated; iii) Hydrophobicity of carbon-electrode is increased due to the long carbon chains of OAI molecules. Merits of i) and ii) help to define the "in situ healing" behavior for "PVSK/carbon" interface.

We have further examined the OAI induced in-situ healing effect by performing "penetration-reaction test". As is shown in **Figure 4**a–c, a thin layer of mesoporous ZrO_2 (meso-ZrO_2) is coated on 3D PVSK layer (ZrO_2 is chosen since it is insulating according to studies in meso CPSCs[50]). Then carbon-electrode is deposited on top. As such, the OAI/IPA from carbon paste could penetrate through the mesoporous layer, then react with the bottom PVSK layer. After the reaction, the carbon-electrode is peeled off, and the remaining PVSK matrix is characterized by XRD and Photoluminescence (PL). As is shown in Figure 4d, a weak peak appears at ~4.5° for the reacted sample, which is due to the formation of 2D PVSK. Besides, diffraction peak (12.7°) of PbI_2 also decreases. The observation coincides well with that shown in Figure 3, clearly reflects the success of in situ healing effect. As shown in Figure 4e,f, two emission regions are monitored for PL test. One is the short-wavelength region of 540–600 nm (excited by 410 nm), and the other is long-wavelength

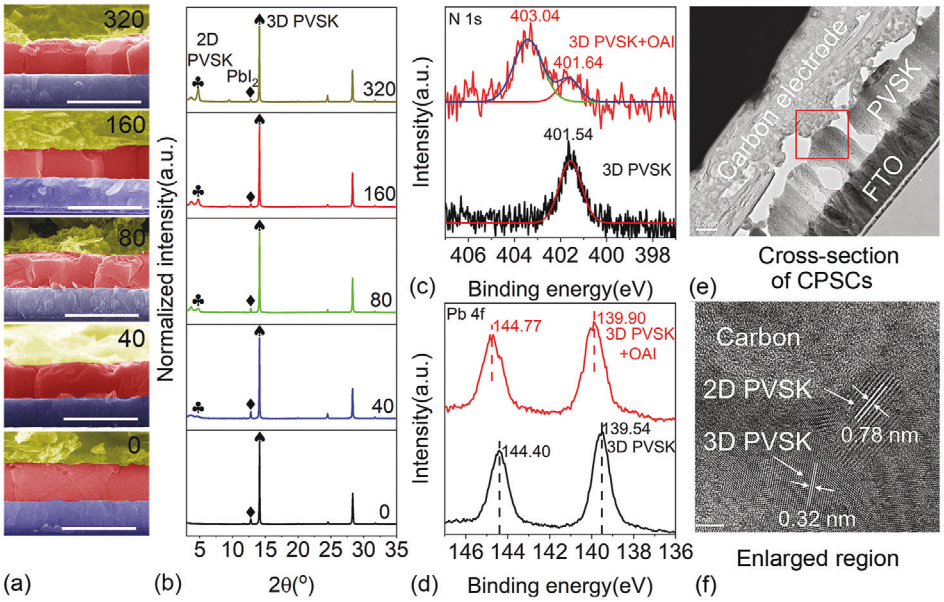

Figure 3. a) Cross-sectional scanning electron microscope (SEM) image of planar CPSCs, from bottom to top the concentration of OAI is 0, 40, 80, 160, and 320 mg, respectively. The scale bar is 1 µm. b) X-ray diffraction (XRD) patterns of PVSK with surface modification basing on OAI. XPS study on PVSK before and after OAI modification: c) N 1s and d) Pb 4f. e) Cross-sectional transmission electron microscope (TEM) image of a typical CPSC with OAI doping, and f) high resolution TEM image of an enlarged region between "PVSK/carbon" interface.

region of 750–850 nm (excited by 600 nm). Clearly, a peak appears at 573.4 nm for the reacted sample, which is ascribed to the characteristic emission peak of 2D PVSK.[51] For the long wavelength region, the peak at ≈808 nm is due to FA basing 3D PVSK.[52] After reaction, the peak intensity rises by more than five times, showing efficient reduction on the nonradioactive recombination, which is due to the defect passivation.

2.2. Strengthen the Moisture Stability Against RH of 85% by "In-situ Healing" Strategy

It is well-known that the PVSK is quite sensitive to moisture. Though carbon-electrode could provide certain protection effect to PVSK, it is still a challenge when faced with heavy moisture. One of the main merits drawn by "in-situ healing" strategy is to

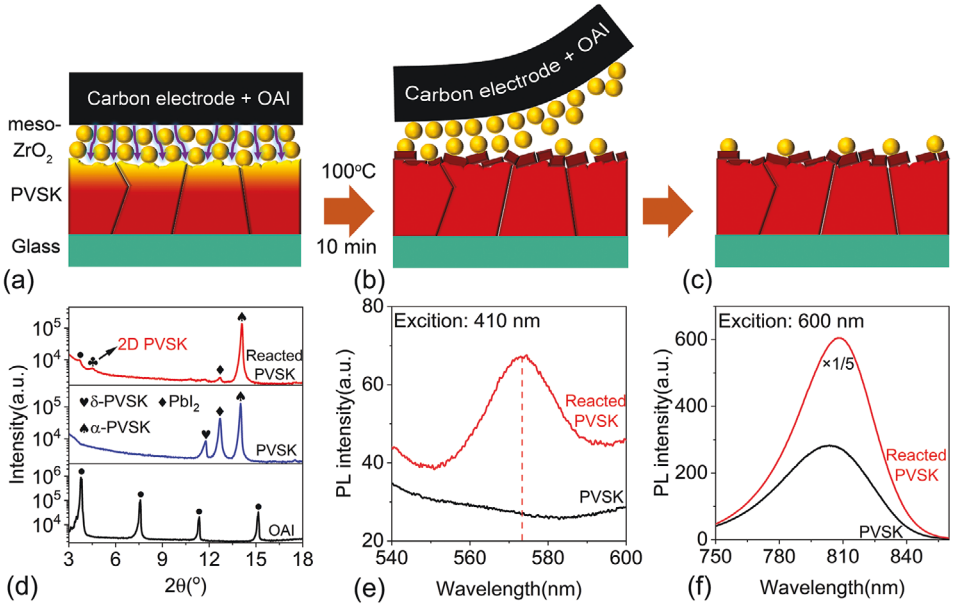

Figure 4. "Penetration-reaction test" to better illustrate the in situ healing effect: a–c) shows the schematic process for the test. d) XRD patterns of PVSK film before and after the reaction, for comparison, XRD of pure OAI powder is also listed. Photoluminance (PL) emission spectra of the PVSK film before and after the reaction: e) 2D PVSK region; and f) 3D PVSK region.

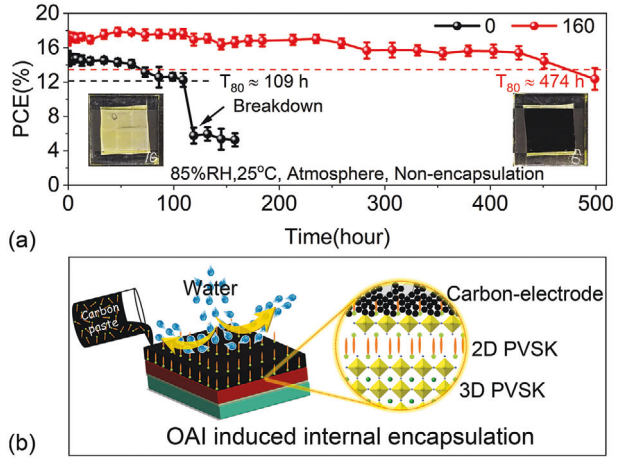

Figure 5. a) Moisture stability test at relative humidity (RH) of 85% (dark, room temperature, un-encapsulated), insets are photo-images of devices peaked after 120 h test. b) Schematic diagram to show the effect of OAI doping on the improved device efficiency and moisture stability.

strengthen the moisture stability of CPSCs against heavy humidity, for example, relative humidity (RH) of 85%. To examine the moisture stability, we treated the CPSCs (without encapsulation) in a closed chamber where the RH was adjusted to 85% (room temperature 25 °C), and then monitor the PCE periodically. As is shown in **Figure 5**a, without doping, PCE of reference devices decreases quickly, even shrinks to 39% of the initial efficiency after 120 h treatment, thus breakdown behavior appears for these reference devices. In contrast, much better stability is harvested for the modified devices. PCE changes quite slightly during the test. For example, even after treating in 85% (RH) environment for 403 h, 93% of initial efficiencies remain. Meanwhile, if T_{80} is defined as the time for the PCE decays to 80% of the original value, one can find that, devices with such "in-situ healing" effect show much longer T_{80} time than reference devices. For example, it is >450 h, more than 4 times to that of reference devices (≈109 h). The improved stability could be also reflected from XRD study, as well as the photo images. Typical devices are picked after being aged for 120 h. As shown in Figure 5a, without OAI doping, the active layer turns bright yellow, showing that the device has degraded. XRD study shows that the active layer mainly consists of PbI_2, with small portion of PVSK (Figure S5, Supporting Information). However, for doped devices (160 mg case), it remains black, and PVSK remains in the active layer, with only a slight portion of PbI_2. As a result, OAI-induced "in-situ healing" has obviously improved the moisture resistance of CPSCs. The improved moisture resistance is due to two facts. First, OAI doping has improved the hydrophobicity of carbon-electrode, which provides a strong barrier for moisture to penetrate. Second, 2D phase PVSK has been formed due to OAI induced "in-situ healing". Owing to the long-chain feature of OAI, it could provide another barrier against the moisture corrosion. Besides, storage-stability has also been recorded by keeping devices in the dark. As shown in Figure S6 (Supporting Information), better stability is observed for OAI-doped devices.

To better understand the observed effect, a schematic diagram is presented in Figure 5b. Clearly, two merits have contributed to the improved moisture stability. One is the increased hydrophobicity of carbon-electrode, the other is the formed 2D phase PVSK at the interface. As such, a kind of "internal encapsulation effect" has been provided along with the "in-situ healing" strategy, rendering it even comparable to sealing techniques. It is well-known that sealing holds an important part in the production cost of electronic devices. Thus the "internal encapsulation effect" brought by OAI could further lower the production cost of CPSCs.

2.3. Improve the Charge Transfer/Recombination Dynamics by "In-situ Healing" Strategy

Charge transfer and recombination dynamics are also studied, with a combination of transient photocurrent/photovoltage (TPC/TPV) decay curves recording. Typical TPC/TPV curves are shown in **Figure 6**a,b, respectively. Charge extraction time (t_d) is collected from the TPC curves. As shown in Figure 6c, t_d starts from 3.05 (± 0.19)μs for pristine CPSCs (without OAI doping), then decreases to 2.79 (± 0.35), 2.25 (± 0.13), and 2.08 (± 0.07) μs at doping of 40, 80, and 160 mg, respectively, though rises to 2.27 (± 0.14) μs at 320 mg. Lifetime of charge carriers in device (τ_{cell}) is fitted from the TPV curves, the results are depicted in Figure 6c. It is 4.05 (± 0.66) μs for reference devices, then increasing to 6.64 (± 0.64), 9.39 (± 1.49), and 11.75 (± 1.07) μs at doping of 40, 80, and 160 mg, respectively, though decreasing to 9.33 (± 1.14) μs at 320 mg. Consequently, charge transfer process is accelerated and recombination is retarded by the "in-situ healing" strategy, while 160 mg doping comes out the fastest transfer and slowest recombination. The improved charge transfer and reduced recombination are due to the in-situ healing effect brought by OAI, or concretely, the improved interfacial contact, reduced defect across the interface between PVSK and carbon-electrode. Dark current–voltage curves of the devices are also tested. As is shown in Figure 6d, relatively higher dark current is observed when there is no OAI-doped; after OAI doping, it decreases obviously. Usually, shunt behavior is relatively easier to observe for the HTM-free devices (also shown in **Figure 7**a), which contributes to the dark current. The reduced dark current is ascribed to the "in-situ healing" behavior, which makes a tightly packed interface. On the other hand, the reduced defects at PVSK (according to formation of 2D phase PVSK), and carbon-electrode (due to the passivation of OAI on carbon) also make contribution to the reduced dark current. Open-circuit voltage (V_{OC})–light intensity (I_P) curve is also tested, and shown in Figure 6e. The so-called ideal factor (n) is fitted according to Equation (2):

$$Voc \propto \frac{nK_BT}{q} \ln I_P \tag{2}$$

where K_B, T, and q are Boltzmann's constant, absolute temperature, and elementary charge, respectively. n of 1.91 is obtained for reference device (without OAI doping in carbon paste), while that of 1.24 is achieved for target device (160 mg OAI doping). The reduced n again shows that recombination is retarded in the device. Mott–Schottky study is performed and capacitance-voltage curves are recorded for planar CPSCs. The result is shown

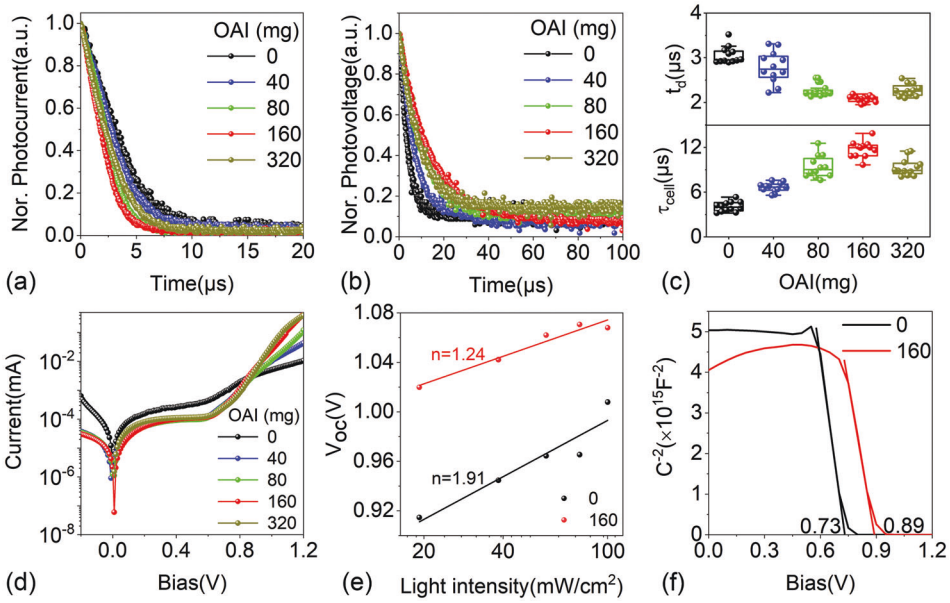

Figure 6. a) Transient photocurrent (TPC) and b) photovoltage (TPV) curve, c) statistics of t_d and τ_{cell} picked from TPC and TPV studies. d) Dark current-voltage curve of planar CPSCs. e) Plotting between V_{OC} and light intensity. f) C^{-2}–V curves recorded from Mott–Schottky study.

in Figure 6f. Built-in potential (V_{bi}) is fitted according to Equation (3)[53]:

$$C^{-2}=\frac{2}{A^2 N_D e\varepsilon\varepsilon_0}(V_{\rm bi}-V) \quad (3)$$

where C, A, N_D, e, and V are capacitance of the device, active area, the number of donors, elementary charge, and applied bias, respectively. It is 0.73 V for reference cell, while 0.89 V for target device. The higher V_{bi} is contributed by "in situ healing" strategy. One is the reduced defects at "perovskite/carbon" interface, and the other is the slightly increased WF of carbon-electrode. Above results show that "in-situ healing" strategy is favorable to device physics of the CPSCs. Similar effects will be seen in the power conversion processes.

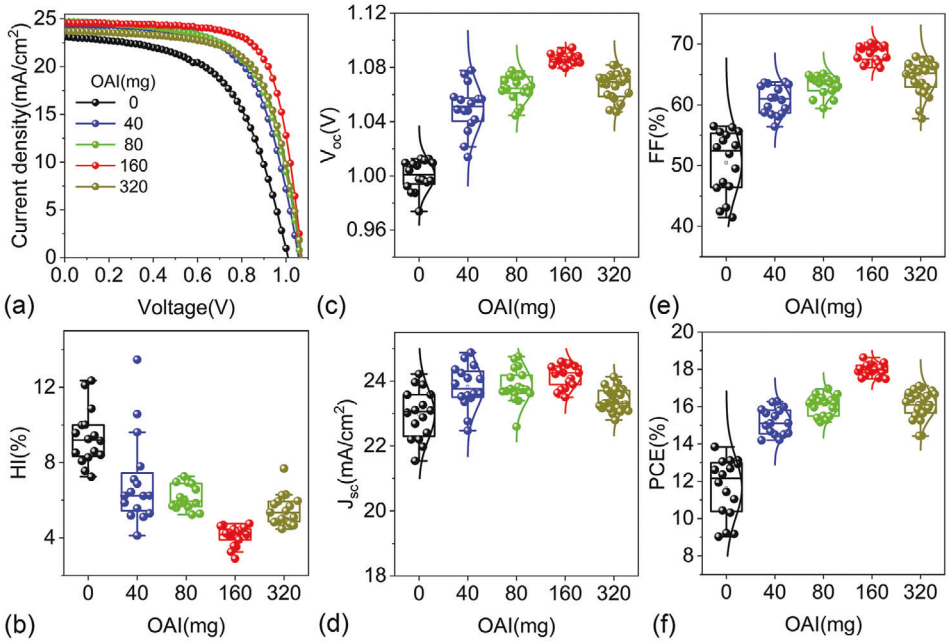

Figure 7. a) Typical current density-voltage curves of planar CPSCs (Reverse scans, AM 1.5 G, 100 mW cm^{-2}). b) Statistics on the HI of planar CPSCs. Statistics on performance parameters with respect to the amount of OAI: c) V_{OC}, d) J_{SC}, e) *FF*, and f) *PCE*. All these parameters are picked from reverse scans.

Table 1. Photovoltaic parameters (measured under AM 1.5G) picked from Figure 7a,c–f.

OAI [mg]	V_{OC} [mV]	J_{SC} [mA cm^{-2}]	FF [%]	PCE [%] (champion ones)
0	1000 (± 11)	22.97 (± 0.77)	50.50 (± 5.27)	11.65 (± 1.59) (13.12)
40	1050 (± 18)	23.82 (± 0.66)	60.78 (± 2.37)	15.20 (± 0.71) (16.24)
80	1064 (± 10)	23.86 (± 0.53)	63.27 (± 1.66)	16.07 (± 0.53) (16.70)
160	1086 (± 4)	24.16 (± 0.35)	68.48 (± 1.35)	17.97 (± 0.32) (18.95)
320	1067 (± 10)	23.41 (± 0.34)	64.45 (± 2.65)	16.10 (± 0.74) (16.93)

2.4. Upgrade the Power Conversion Efficiency of CPSCs by "In Situ Healing" Strategy

Another functionality brought by the "in-situ healing" strategy is the largely boosted PCE for the hole-conductor-free, planar-structured CPSCs. Typical current density–voltage (*JV*) curves are shown in Figure 7a. Without OAI doping, shunt behavior appears; after doping, normal *JV* curves come back. Statistics are carried out for the performance parameters V_{OC}, J_{SC}, *FF*, and *PCE*, which are shown in Figure 7c–f, respectively. Clearly, after OAI doping, all of the four performance parameters have been improved. As OAI from 0 to 160 mg, V_{OC} increases from 1000 (± 11) to 1086 (± 4) mV; J_{SC} rises from 22.97 (± 0.77) to 24.16 (± 0.35) mA cm^{-2}; *FF* promotes from 50.50 (± 5.27) to 68.48 (± 1.35) %; finally, *PCE* improves from 11.65 (± 1.59) to 17.97 (± 0.32) %. The photovoltaic parameters of typical cells at different doping levels are collected in **Table 1**. For example, performance parameters of 1.01 V (V_{OC}), 23.10 mA cm^{-2} (J_{SC}), 56.30% (*FF*), and 13.12% (*PCE*) are obtained for reference devices. Then for moderate doping devices (160 mg), V_{OC} of 1.07 V, J_{SC} of 24.56 mA cm^{-2}, *FF* of 72.22%, and *PCE* of 18.95% are harvested. One can see that the main improvements come from V_{OC} and *FF*. For example, an increment of 10% has been obtained for V_{OC}, and that of 40% has been achieved for *FF*. The improvement is due to the "in-situ healing" at "PVSK/carbon" interface, or the reduced defect to both PVSK and carbon-electrode, giving elevated WF of carbon-electrode in addition. According to device physics, an increase in WF would downshift the Fermi level, which then reduces the energy gap between the carbon-electrode and PVSK. As a result, the charge transfer process is favored, and recombination is retarded, by which V_{OC} and *FF* are upgraded. Besides, the strengthened interfacial contact between PVSK and carbon-electrode could also accelerate the charge transfer process, which is favorable for *FF*. It is noted that OAI doping could also reduce the hysteresis behavior. For comparison, Hysteresis index (*HI*) is estimated according to Equation (4):

$$HI = \frac{PCE^{+} - PCE^{-}}{PCE^{+} + PCE^{-}} \times 100\% \quad (4)$$

Then statistics is performed on *HI*, which is shown in Figure 7b. One can see that smaller *HI* is achieved after OAI doping, while 160 mg doping comes out with the smallest *HI*. Indeed, hysteresis is a common behavior seen in PSCs, it relates to ion migration, which is sensitive to defects.[54] The reduced *HI* is due to the reduced defect by OAI doping, which helps to form 2D phase structure on PVSK surface.

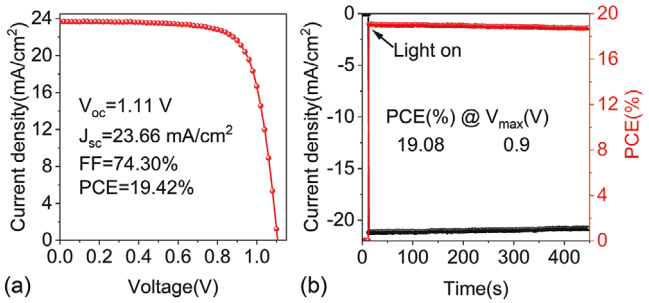

Figure 8. a) Typical JV curve (reverse scan) of the hole-conductor-free, planar CPSCs with PbI_2-doped by SiO_2 nanoparticles. b) Quasi-maximum power point tracking (Q-MPPT) curve. Note carbon paste is doped by 160 mg OAI.

Previously, Meng and Shi groups found that adding spiro-OMeTAD basing HTM was helpful to improve device efficiencies.[24,29] Here, we also check the availability of the "in-situ healing" effect when HTM is incorporated. Typically, spiro-OMeTAD basing HTM is deposited on PVSK, after that carbon-electrode is coated . Typical JV curves and related performance parameters are listed in Figure S7 (Supporting Information). CPSCs involving spiro-OMeTAD basing HTM produces PCE of 15.14 (±0.33) %, compared to 11.65 (±1.59) % of the control devices. Such behavior implies that, OAI molecules could penetrate through the Spiro-OMeTAD layer, and also triggered the in-situ healing behavior. However, it seems that the healing behavior is more efficient when Spiro-OMeTAD is not used. Such phenomenon is quite interesting, butmore works are worthy to be done by considering the interaction between materials at the complex interface of "PVSK/HTM/Carbon-electrode". In more, other kinds of HTM could also be considered, so as to examine the compatibility of the in situ healing strategy.

The PCE could be further upgraded by doping SiO_2 nanoparticle in PVSK layer, like that done in our previous report.[55] As is shown in **Figure 8**a, a *PCE* of 19.42% is obtained, with V_{OC} of 1.11 V, and FF of 74.30%.The V_{OC} is comparable to CPSCs using spiro-OMeTAD as HTM,[25,29] and even close to that of metal electrode-basing devices whereas HTM (like spiro-OMeTAD) is adopted.[56] The efficiency is comparable to that recently reported for planar CPSCs.[57] Note that such V_{OC} is obtained in a hole-conductor-free device. Again, it shows that, by suitably tuning the interfacial structure between "PVSK/carbon", it is possible to achieve high open-circuit voltage. As such, the "in-situ healing" strategy is quite appealing for the optimization on this interface. In addition, quasi-maximum power point tracking (Q-MPPT) is performed (Figure 8b), which observes a stabilized efficiency at 18.7% after ≈400s test, ≈96.3% of the JV-recorded value. External quantum efficiency (EQE) spectra is also tested, the results is shown in Figure S8 (Supporting Information), as well as the related JV curves. The integrated J_{SC} is 22.51 mA cm^{-2}, which matches 95% to the JV-recorded value.

3. Conclusion

In summary, "in-situ healing" effect is observed at the "perovskite/carbon" interface, through doping OAI in carbon paste. Due to this effect, defects are reduced for both carbon-electrode

and PVSK layer, interfacial contact between PVSK and carbon-electrode is strengthened, and the work function of carbon-electrode is slightly elevated. Accordingly, charge recombination is retarded, and charge transfer is accelerated, which helps to upgrade the PCE to 19.42% (stabilized at 18.7%). Moreover, OAI doping helps to increase the moisture resistance of devices at RH of 85%, rendering a kind of "internal encapsulation effect", which is helpful to reduce the production cost.

4. Experimental Section

Materials: Graphite powder (99.85%), tin (II) chloride dehydrate (98%) were purchased from Sinopharm (Shanghai). Carbon black (Ketjen Black, ECP600JD, Japan LION) was purchased from Suzhou Yilongsheng Energy Technology Co., Ltd. Hydroxypropyl cellulose was purchased from Aladdin. Dimethylformamide (DMF), dimethyl sulfoxide (DMSO), isopropyl alcohol (IPA) was purchased from Sigma–Aldrich. Lead (II) iodide (PbI_2) and conductive glass (FTO) were purchased from Advanced Election Technology Co., Ltd. Octylammonium iodide (OAI), Formamidinium iodide (FAI), methylammonium bromide (MABr), methylammonium chloride (MACl) were purchased from Xi'an Polymer Light Technology Corp. All reagents were used as received.

Material Synthesis: *Carbon paste*: Carbon paste was prepared by ball milling 6 g graphite, 0.75 g carbon black, 1 g hydroxypropyl cellulose in 25 mL IPA for 24 h. Certain amount of OAI was added to the carbon paste, for example, 0, 40, 80, 160, and 320 mg, respectively.

Perovskite precursor: PbI_2 precursor was prepared by dissolving 553 mg PbI_2 in 1 mL solvent mixture between DMF and DMSO (volume ratio = 9.5:0.5), being stirred at 70 °C for overnight. Organic salt solution was prepared by dissolving 60 mg FAI, 6 mg MABr and 8.2 mg MACl in 1 mL IPA.

Device fabrication: CPSCs were prepared using FTO as substrates. Treatment on FTO, and then the deposition of SnO_2, PbI_2, and hence the PVSK layer are all the same to like described before.[58] Carbon-electrode was deposited on top of PVSK layer by doctoral blading using carbon paste and then annealed at 100 °C for 10 min in atmospheric environment.

SiO_2 nanoparticle doping in PVSK: SiO_2 nanoparticles was dispersed in DMF by ultrasonic treatment (Scientz-IID, 380 W) for 10 min to prepare stock precursor. Then certain amount of SiO_2 stock precursor was added to PbI_2 solution, with molar ratio of 8% of PbI_2.[55]

Materials characterization and device performance evaluation: Morphological properties were performed on scanning electron microscopy (SEM, TESCAN MIRA3 LMU). Chemical interaction of materials was conducted by Fourier transform infrared (FTIR, Nicolet 6700). The crystallographic structure of PVSK was detected by X-ray diffraction (XRD, D8 Advance, Bruker). High-resolution transmission electron microscope (HRTEM) was characterized on arm200f. X-ray photoemission spectrum (XPS) is recorded by SPECS XR-MF, with monochromatized Al source ($h\nu$ = 1486.6 eV). Work function of carbon electrode was characterized by Ultraviolet photoemission spectroscopy (UPS, thermofisher escalab 250xi) on equipped with monochromatized He I source ($h\nu$ = 21.22 eV). Transient photovoltage/photocurrent (TPV/TPC) decay curves were measured by a home-made system including a digital oscilloscope (DSO-X 3104A, Keysight) and N_2 laser (NL100, 337 nm, Stanford), like that described before.[59] Current density-voltage curves were recorded by a digital sourcemeter (model 2400, Keithley Inc.) under simulated illumination (Enlitech SS-F7-3A, AM1.5G). Moisture stability was tested in damp oven (PL-80, Hongzhan Technology).

Supporting Information

Supporting Information is available from the Wiley Online Library or from the author.

Acknowledgements

C.Z. thanks the financial support of the National Natural Science Foundation of China (NSFC, no. 61774170), the Natural Science Foundation of Hunan Province (no. 2020JJ4759), and the Scientific Research Project of Education Department of Hunan Province (22A0005). Y.G. acknowledges the support from the National Science Foundation, United States (NSF no. DMR-1903962).

Conflict of Interest

The authors declare no conflict of interest.

Data Availability Statement

The data that support the findings of this study are available in the article, as well as in the supporting information.

Keywords

carbon electrodes, hole conductor-free, moisture, perovskite solar cells, stability

Received: June 7, 2023
Revised: September 6, 2023
Published online:

[1] A. Kojima, K. Teshima, Y. Shirai, T. Miyasaka, *J. Am. Chem. Soc.* **2009**, *131*, 6050.
[2] H.-S. Kim, C.-R. Lee, J.-H. Im, K.-B. Lee, T. Moehl, A. Marchioro, S.-J. Moon, R. Humphry-Baker, J.-H. Yum, J. E. Moser, M. Grätzel, N.-G. Park, *Sci. Rep.* **2012**, *2*, 591.
[3] M. Jeong, I. W. Choi, E. M. Go, Y. Cho, M. Kim, B. Lee, S. Jeong, Y. Jo, H. W. Choi, J. Lee, J.-H. Bae, S. K. Kwak, D. S. Kim, C. Yang, *Science* **2020**, *369*, 1615.
[4] Y. Zhao, F. Ma, Z. Qu, S. Yu, T. Shen, H.-X. Deng, X. Chu, X. Peng, Y. Yuan, X. Zhang, J. You, *Science* **2022**, *377*, 531.
[5] https://www.nrel.gov/pv/cell-efficiency.html
[6] L. Meng, J. You, Y. Yang, *Nat. Commun.* **2018**, *9*, 5265.
[7] Y. Kato, L. K. Ono, M. V. Lee, S. Wang, S. R. Raga, Y. Qi, *Adv. Mater. Interfaces* **2015**, *2*, 1500195.
[8] C. Besleaga, L. E. Abramiuc, V. Stancu, A. G. Tomulescu, M. Sima, L. Trinca, N. Plugaru, L. Pintilie, G. A. Nemnes, M. Iliescu, H. G. Svavarsson, A. Manolescu, I. Pintilie, *J. Phys. Chem. Lett.* **2016**, *7*, 5168.
[9] A. K. Jena, Y. Numata, M. Ikegami, T. Miyasaka, *J. Mater. Chem. A* **2018**, *6*, 2219.
[10] T. Zhang, F. Wang, H.-B. Kim, I.-W. Choi, C. Wang, E. Cho, R. Konefal, Y. Puttisong, K. Terado, L. Kobera, M. Chen, M. Yang, S. Bai, B. Yang, J. Suo, S.-C. Yang, X. Liu, F. Fu, H. Yoshida, W. M. Chen, J. Brus, V. Coropceanu, A. Hagfeldt, J.-L. Brédas, M. Fahlman, D. S. Kim, Z. Hu, F. Gao, *Science* **2022**, *377*, 495.
[11] Z. Ku, Y. Rong, M. Xu, T. Liu, H. Han, *Sci. Rep.* **2013**, *3*, 3132.
[12] M. Uda, A. Nakamura, T. Yamamoto, Y. Fujimoto, *J. Electron Spectrosc. Relat. Phenom.* **1998**, *88–91*, 643.
[13] A. Mei, X. Li, L. Liu, Z. Ku, T. Liu, Y. Rong, M. Xu, M. Hu, J. Chen, Y. Yang, M. Grätzel, H. Han, *Science* **2014**, *345*, 295.
[14] Y. Yang, Z. Liu, W. K. Ng, L. Zhang, H. Zhang, X. Meng, Y. Bai, S. Xiao, T. Zhang, C. Hu, K. S. Wong, S. Yang, *Adv. Funct. Mater.* **2019**, *29*, 1806506.

[15] J. Yan, S. Lin, X. Qiu, H. Chen, K. Li, Y. Yuan, M. Long, B. Yang, Y. Gao, C. Zhou, *Appl. Phys. Lett.* **2019**, *114*, 103503.
[16] J. Liu, Q. Zhou, N. K. Thein, L. Tian, D. Jia, E. M. J. Johansson, X. Zhang, *J. Mater. Chem. A* **2019**, *7*, 13777.
[17] S. Liu, D. Zhang, Y. Sheng, W. Zhang, Z. Qin, M. Qin, S. Li, Y. Wang, C. Gao, Q. Wang, Y. Ming, C. Liu, K. Yang, Q. Huang, J. Qi, Q. Gao, K. Chen, Y. Hu, Y. Rong, X. Lu, A. Mei, H. Han, *Fundam. Res.* **2022**, *2*, 276.
[18] H. Zhou, Y. Shi, K. Wang, Q. Dong, X. Bai, Y. Xing, Y. Du, T. Ma, *J. Phys. Chem. C* **2015**, *119*, 4600.
[19] T. Tian, J.-X. Zhong, M. Yang, W. Feng, C. Zhang, W. Zhang, Y. Abdi, L. Wang, B.-X. Lei, W.-Q. Wu, *Angew. Chem., Int. Ed.* **2021**, *60*, 23735.
[20] T. Ye, Y. Hou, A. Nozariasbmarz, D. Yang, J. Yoon, L. Zheng, K. Wang, K. Wang, S. Ramakrishna, S. Priya, *ACS Energy Lett.* **2021**, *6*, 3044.
[21] A. Mei, Y. Sheng, Y. Ming, Y. Hu, Y. Rong, W. Zhang, S. Luo, G. Na, C. Tian, X. Hou, Y. Xiong, Z. Zhang, S. Liu, S. Uchida, T.-W. Kim, Y. Yuan, L. Zhang, Y. Zhou, H. Han, *Joule* **2020**, *4*, 2646.
[22] F. Meng, Y. Li, L. Gao, A. Liu, Y. Li, T. Wang, C. Zhang, M. Fan, G. Wei, T. Ma, *ACS Appl. Mater. Interfaces* **2020**, *12*, 34479.
[23] Y. Yang, M. T. Hoang, D. Yao, N. D. Pham, V. T. Tiong, X. Wang, W. Sun, H. Wang, *Sol. Energy Mater. Sol. Cells* **2020**, *210*, 110517.
[24] H. Zhang, J. Xiao, J. Shi, H. Su, Y. Luo, D. Li, H. Wu, Y.-B. Cheng, Q. Meng, *Adv. Funct. Mater.* **2018**, *28*, 1802985.
[25] H. Zhang, Y. Li, S. Tan, Z. Chen, K. Song, S. Huang, J. Shi, Y. Luo, D. Li, Q. Meng, *J. Colloid Interface Sci.* **2022**, *608*, 3151.
[26] Q.-Q. Chu, B. Ding, Q. Qiu, Y. Liu, C.-X. Li, C.-J. Li, G.-J. Yang, B. Fang, *J. Mater. Chem. A* **2018**, *6*, 8271.
[27] N. Arora, M. I. Dar, S. Akin, R. Uchida, T. Baumeler, Y. Liu, S. M. Zakeeruddin, M. Grätzel, *Small* **2019**, *15*, e1904746.
[28] Y. Li, X. Lu, Y. Mei, C. Dong, D. T. Gangadharan, K. Liu, Z. Wang, S. Qu, M. I. Saidaminov, W. Zhang, F. Tan, *Adv. Funct. Mater.* **2023**, *33*, 2301920.
[29] Y. Wang, W. Li, Y. Yin, M. Wang, W. Cai, Y. Shi, J. Guo, W. Shang, C. Zhang, Q. Dong, H. Ma, J. Liu, W. Tian, S. Jin, J. Bian, Y. Shi, *Adv. Funct. Mater.* **2022**, *32*, 2204831.
[30] S. Zouhair, S.-M. Yoo, D. Bogachuk, J. P. Herterich, J. Lim, H. Kanda, B. Son, H. J. Yun, U. Würfel, A. Chahboun, M. K. Nazeeruddin, A. Hinsch, L. Wagner, H. Kim, *Adv. Energy Mater.* **2022**, *12*, 2200837.
[31] X. Chen, Y. Xia, Z. Zheng, X. Xiao, C. Ling, M. Xia, Y. Hu, A. Mei, R. Cheacharoen, Y. Rong, H. Han, *Chem. Mater.* **2022**, *34*, 728.
[32] X. Zheng, H. Chen, Q. Li, Y. Yang, Z. Wei, Y. Bai, Y. Qiu, D. Zhou, K. S. Wong, S. Yang, *Nano Lett.* **2017**, *17*, 2496.
[33] C. Tian, A. Mei, S. Zhang, H. Tian, S. Liu, F. Qin, Y. Xiong, Y. Rong, Y. Hu, Y. Zhou, S. Xie, H. Han, *Nano Energy* **2018**, *53*, 160.
[34] C. Zhou, S. Lin, *Sol. RRL* **2019**, *4*, 1900190.
[35] H. Kim, S.-U. Lee, D. Y. Lee, M. J. Paik, H. Na, J. Lee, S. I. Seok, *Adv. Energy Mater.* **2019**, *9*, 1902740.
[36] F. Zhang, S. Y. Park, C. Yao, H. Lu, S. P. Dunfield, C. Xiao, S. Ulicná, X. Zhao, L. Du Hill, X. Chen, X. Wang, L. E. Mundt, K. H. Stone, L. T. Schelhas, G. Teeter, S. Parkin, E. L. Ratcliff, Y.-L. Loo, J. J. Berry, M. C. Beard, Y. Yan, B. W. Larson, K. Zhu, *Science* **2022**, *375*, 71.
[37] S. Sidhik, Y. Wang, M. De Siena, R. Asadpour, A. J. Torma, T. Terlier, K. Ho, W. Li, A. B. Puthirath, X. Shuai, A. Agrawal, B. Traore, M. Jones, R. Giridharagopal, P. M. Ajayan, J. Strzalka, D. S. Ginger, C. Katan, M. A. Alam, J. Even, M. G. Kanatzidis, A. D. Mohite, *Science* **2022**, *377*, 1425.
[38] C. Liu, C. Gao, W. Wang, X. Wang, Y. Wang, W. Hu, Y. Rong, Y. Hu, L. Guo, A. Mei, H. Han, *Sol. RRL* **2021**, *5*, 2100333.
[39] X. Chen, X. Wang, D. Fang, *Fullerenes, Nanotubes Carbon Nanostruct.* **2020**, *28*, 1048.
[40] F. Jaouen, S. Marcotte, J.-P. Dodelet, G. Lindbergh, *J. Phys. Chem. B* **2003**, *107*, 1376.
[41] J.-O. Müller, D. S. Su, U. Wild, R. Schlögl, *Phys. Chem. Chem. Phys.* **2007**, *9*, 4018.
[42] A. Cros, *J. Electron Spectrosc. Relat. Phenom.* **1992**, *59*, 1.
[43] H. Tetsuka, R. Asahi, A. Nagoya, K. Okamoto, I. Tajima, R. Ohta, A. Okamoto, *Adv. Mater.* **2012**, *24*, 5333.
[44] Y. Gao, *Mater. Sci. Eng.* **2010**, *68*, 39.
[45] D. H. Cao, C. C. Stoumpos, O. K. Farha, J. T. Hupp, M. G. Kanatzidis, *J. Am. Chem. Soc.* **2015**, *137*, 7843.
[46] L. Tan, L. Shen, P. Song, Y. Luo, L. Zheng, C. Tian, L. Xie, J. Yang, Z. Wei, *Adv. Energy Sustainability Res.* **2023**, *4*, 2200189.
[47] C. Zhang, S. Wu, L. Tao, G. M. Arumugam, C. Liu, Z. Wang, S. Zhu, Y. Yang, J. Lin, X. Liu, R. E. I. Schropp, Y. Mai, *Adv. Energy Mater.* **2020**, *10*, 2002004.
[48] J. Jeong, M. Kim, J. Seo, H. Lu, P. Ahlawat, A. Mishra, Y. Yang, M. A. Hope, F. T. Eickemeyer, M. Kim, Y. J. Yoon, I. W. Choi, B. P. Darwich, S. J. Choi, Y. Jo, J. H. Lee, B. Walker, S. M. Zakeeruddin, L. Emsley, U. Rothlisberger, A. Hagfeldt, D. S. Kim, M. Grätzel, J. Y. Kim, *Nature* **2021**, *592*, 381.
[49] J.-W. Lee, S. Tan, S. I. Seok, Y. Yang, N.-G. Park, *Science* **2022**, *375*, eabj1186.
[50] D. Guo, J. Ma, S. Lin, X. Guo, H. Huang, D. Kong, F. Xu, Y. Gao, W. Zhang, Y. Hu, C. Zhou, *Appl. Phys. Lett.* **2022**, *120*, 263502.
[51] L. Shen, P. Song, L. Zheng, L. Wang, X. Zhang, K. Liu, Y. Liang, W. Tian, Y. Luo, J. Qiu, C. Tian, L. Xie, Z. Wei, *Adv. Mater.* **2023**, https://doi.org/10.1002/adma.202301624.
[52] S. Wu, S. Lin, Z. Shi, De' Guo, H. Huang, X. Zhou, D. Zhang, K. Zhou, W. Zhang, Y. Hu, C. Zhou, *Small* **2023**, *19*, e2207848.
[53] K. Gelderman, L. Lee, S. W. Donne, *J. Chem. Educ.* **2007**, *84*, 685.
[54] Y. Yuan, Q. Wang, Y. Shao, H. Lu, T. Li, A. Gruverman, J. Huang, *Adv. Energy Mater.* **2016**, *6*, 1501803.
[55] Z. Liang, B. Yang, A. Mei, S. Lin, H. Han, Y. Yuan, H. Xie, Y. Gao, C. Zhou, *Chin. Phys. B* **2020**, *29*, 078401.
[56] S. Lin, P. Xia, S. Wu, W. Zhang, Y. Hu, B. Liu, D. Kong, H. Huang, Y. Gao, C. Zhou, *Appl. Phys. Lett.* **2022**, *120*, 103503.
[57] Y. Wang, L. Li, Z. Wu, R. Zhang, J. Hong, J. Zhang, H. Rao, Z. Pan, X. Zhong, *Angew. Chem., Int. Ed.* **2023**, *62*, e202302342.
[58] P. Xia, De' Guo, S. Lin, S. Liu, H. Huang, D. Kong, Y. Gao, W. Zhang, Y. Hu, C. Zhou, *Sol. RRL* **2021**, *5*, 2100408.
[59] S. Lin, S. Wu, De' Guo, H. Huang, X. Zhou, D. Zhang, K. Zhou, W. Zhang, Y. Hu, Y. Gao, C. Zhou, *Small Methods* **2023**, *7*, e2201663.